IMPACT OF GROUND FLOOR OPENINGS PERCENTAGE ON THE DYNAMIC RESPONSE OF TYPICAL DUTCH URM CAVITY WALL STRUCTURES

D. Malomo[1,2], C. Morandini[3], H. Crowley[4], Rui Pinho[2,3], A. Penna[3]

[1] Department of Civil Engineering and Applied Mechanics, McGill University, Canada.
E-mail: daniele.malomo@mcgill.ca (corresponding author)
[2] Modelling and Structural Analysis Konsulting (Mosayk Ltd), Pavia, Italy.
[3]Department of Civil Engineering and Architecture, University of Pavia, Italy.
[4] Seismic Risk Consultant, Pavia, Italy.

ABSTRACT

Unreinforced masonry (URM) buildings with cavity walls, typically constituted by the assembly of a loadbearing inner leaf weakly coupled to an outer veneer with no structural functions, are widely present in a number of regions exposed to tectonic or induced seismicity, including the Groningen province (The Netherlands), which has lately experienced low-intensity ground shaking due to natural gas extraction. Recently, experimental evidence has shown that the lack of seismic details, and, above all, the presence of large ground floor openings, makes these structures particularly vulnerable towards horizontal actions. In this endeavour, advanced discrete element models, developed within the framework of the Applied Element Method (AEM), are employed to investigate numerically the impact of ground floor openings percentage on the dynamic behaviour of cavity wall systems representative of the typical Dutch terraced houses construction, namely low-rise residential URM buildings with rigid floor diaphragms and timber roof. Firstly, the model is validated through comparison with a shake-table test of a full-scale building specimen, tested up to near-collapse. Then, a comprehensive numerical study, which featured several combinations of ground-floor openings and the application of various acceleration time-histories up to complete collapse, is undertaken. The ensuing results allowed a comparison of the fragility associated with each of the considered openings layouts, showing how the presence of large ground floor openings may significantly increase the seismic vulnerability of typical URM Dutch terraced houses.

Keywords: unreinforced masonry; cavity wall systems; openings; shake-table; Applied Element Method

1. INTRODUCTION

The cavity wall construction technique is typical of Central and Northern European regions (though it is now widely seen also in a number of other countries around the world, such e.g. China, USA, New Zealand (Dizhur et al. 2013; Zhang et al. 2016; Desai 2017), including the Groningen province in The Netherlands, where it usually consists of an assembly of a loadbearing inner unreinforced masonry (URM) calcium-silicate (CS) brick panels plus an external clay (CL) brick building envelope aimed at providing protection against atmospheric agents and thermal insulation in addition to the characteristic aesthetic appearance. These two masonry wythes are typically weakly coupled by metal connectors (or tie elements). Because of the intrinsic vulnerability of URM cavity wall systems, they became in recent years the focus of various experimental (e.g. Dizhur et al. 2017; Derakhshan et al. 2018; Graziotti et al. 2019a) and numerical (e.g. Tomassetti et al. 2018; Kallioras et al. 2019; D'Altri et al. 2019a; Malomo et al. 2020a) research endeavours. In this framework, of particular interest is the situation of the Groningen region, not historically-prone to tectonic earthquakes but now exposed to low-intensity ground motions due to natural gas extraction. Indeed, a relevant part of the Groningen building stock is constituted by URM cavity wall structures (see **Figure 1**, where one of the end units – usually taken as a reference for the design of full-scale building specimens, as discussed in the following – is highlighted in red), which typically come in the form of contiguous low-rise constructions (hereinafter referred to as *terraced houses*) characterised by large ground floor openings, rigid floor diaphragms and timber roof.

Despite the need for detailed numerical analyses of the collapse response of cavity wall terraced house buildings for supporting the development seismic risk models (e.g. van Elk 2019) in regions where these structural types are most widespread, they were not readily available in the literature. Indeed, their validation required shake-table tests on complete structural systems that only now have become available, through the experimental campaign cited above. Further, since the local interaction among in-plane and out-of-plane (OOP) loaded components often influences the global response of cavity wall systems, the use of simplified models (e.g. Penna et al. 2014; Raka et al. 2015; Sangirardi et al. 2019), which often neglect the contribution of OOP-loaded members, seems to be not generally applicable.

Malomo et al. (2020) – received 23 Mar 2020, revised 28 Sept 2020, accepted 6 Oct 2020

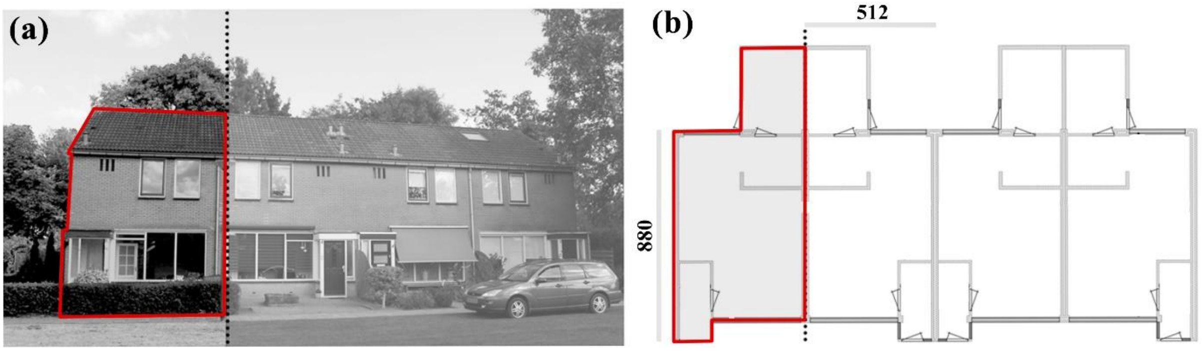

Figure 1. (a) Front and (b) plan views of a typical Dutch URM terraced house (adapted from Graziotti et al. 2017) – the red envelopes indicate the right-side end unit

Similarly, as extensively discussed in Grunwald et al. (2018), the application of most of the typically-employed continuum-based advanced numerical approaches (e.g. the Finite Element Method, FEM) to the collapse simulation of complex structures might lead to inadequate results. This notwithstanding, satisfactory results have been obtained using FEM micro (Petracca et al. 2017; Abdulla et al. 2017) and meso-scale (Aref and Dolatshahi 2013; Giambanco et al. 2018) modelling strategies for the analysis of pre-collapse damage states, as comprehensively discussed in (D'Altri et al. 2019b). On the other hand, several applications (Pulatsu et al. 2016; Galvez et al. 2018b; Godio and Beyer 2019; Portioli 2019; Masi et al. 2020) have shown that e.g. Distinct Element (DEM) and Rigid Bodies and Spring models (RBSM) (see Lemos 2007), being able to account explicitly for the discrete nature of masonry, are capable of duly representing the mutual interaction among various bodies, as well as separation, impact and frictional phenomena. However, although some promising hybrid modelling strategies have been recently proposed (e.g. Pantò et al. 2017; Chácara et al. 2018; Malomo et al. 2019a), obtaining results in a reasonable timeframe is still an open challenge. A similar but more computationally efficient numerical technique is the Applied Element Method (AEM), initially conceived by Meguro and Tagel-Din (2000) for simulating controlled demolition and collapse of steel and reinforced concrete (RC) structures (e.g. Salem et al. 2016; Calvi et al. 2019). As most of the RBSM, the AEM is based on the mechanical interaction among rigid blocks connected by nonlinear spring layers, carrying only mass and damping of the system. However, unlike RBSM (see Furukawa et al. 2012), the recontact between neighbouring elements initially not in contact is allowed. This is an essential feature for collapse analysis, which enabled various researchers to develop AEM-based models capable of satisfactorily reproducing the response of large-scale systems up to complete failure (e.g. Karbassi and Nollet 2013; Domaneschi et al. 2019; Malomo et al. 2020c).

As a result of all of the above, the AEM was employed in this work for investigating numerically the influence of ground floor openings percentage on the dynamic behaviour and collapse capacity of full-scale terraced house structures with cavity walls, rigid diaphragms and timber roof. To this end, leverage was made on the comprehensive experimental campaign described by Graziotti et al. (2019a), which featured, in addition to static/dynamic testing of cavity wall components (Graziotti et al. 2016b, a, 2019b) and sub-structures (Tomassetti et al. 2019a, b), also the shake-table testing of two full-scale cavity wall two-story building prototypes representative of the end-unit of a set of typical Dutch terraced houses; EUC-BUILD1 (Graziotti et al. 2017) and EUC-BUILD6 (Miglietta et al. 2019); the main distinction between such test specimens was in the size of their ground-floor openings, which were purposely wider in the case of EUC-BUILD6. Taking also advantage of the findings in Malomo et al. (2020b), where adequate agreement among experimental outcomes and numerical counterparts of shake-table-tested cavity wall building specimens (including EUC-BUILD1) has been found, a refined AEM model of EUC-BUILD6 was herein developed and preliminarily calibrated through comparison against the available experimental results. Given the encouraging results obtained, analogous assumptions were also considered for the development of a number of models in which, parametrically, the area of ground floor openings was varied. For each configuration, the predicted damage distribution, failure modes and collapse capacities, as well as the inferred total base shear, significantly differed from one to another, underlining the impact that the extent of ground floor openings can have on the dynamic performance of cavity wall buildings. Finally, leveraging upon the results of the abovementioned analyses, a comparative assessment of the effect that the openings configuration has on the fragility of the considered case-study was also undertaken.

2. APPLIED ELEMENT MODELLING OF URM CAVITY WALL SYSTEMS

Within the AEM framework, three-dimensional elements are idealised as an assembly of rigid bodies, characterised by six degrees of freedom. Connection is provided by zero-thickness nonlinear interface springs (with normal (k_{ni}) and shear (k_{si}) stiffness, Eqs. (1)-(2)) uniformly distributed along the contact surfaces, in which the mechanical properties of the system are lumped. Interface forces among adjacent units are inferred by multiplying the local stiffness matrix with the displacement vector terms (or vice-versa, in the case of displacement-controlled problems). As shown in e.g. Malomo et al. (2018), to which interested readers are referred for further details, global stiffness matrix of the whole structure can be obtained by assembling the matrices referred to each couple of units in the considered directions. The actual masonry texture of CS/CL cavity wall members (which usually feature a standard running bond pattern) can be explicitly represented using such a simplified micro-modelling approach, as depicted in **Figure 2**(a). From the latter, where E_u, G_u, E_{mo} and G_{mo} are the unit and mortar Young's and shear moduli respectively, while j and d stand for the spring number along y and z-direction respectively, it can be gathered that k_{ni} and k_{si} are computed assuming unit and mortar springs arranged in series. The interface stiffnesses k_{nu} and k_{su} of unit-to-unit spring layers, instead, can be inferred using Eqs. (3)-(4). It is however noted that since the effect of brick failures was not particularly predominant in the response of EUC-BUILD6, bricks were herein modelled as fully-rigid, without any internal subdivision (see **Figure 2**(a)).

$$k_{ni} = \sum_{i=1}^{j} \left(\frac{l_u - t_{mo}}{E_u \, d \left(\frac{t_u}{j}\right)} + \frac{t_{mo}}{E_{mo} \, d \left(\frac{t_u}{j}\right)} \right)^{-1} \tag{1}$$

$$k_{si} = \sum_{i=1}^{j} \left(\frac{l_u - t_{mo}}{G_u \, d \left(\frac{t_b}{j}\right)} + \frac{t_{mo}}{G_{mo} \, d \left(\frac{t_u}{j}\right)} \right)^{-1} \tag{2}$$

$$k_{nu} = \sum_{i=1}^{j} \left(\frac{E_u \, d \left(\frac{t_u}{j}\right)}{l_e} \right) \tag{3}$$

$$k_{su} = \sum_{i=1}^{j} \left(\frac{G_u \, d \left(\frac{t_u}{j}\right)}{l_e} \right) \tag{4}$$

In the nonlinear range, a simplified version of the elastic-perfectly-plastic fracture model conceived by El-Kashif and Maekawa (2004) is typically used for representing the effect of cyclic damage due to uniaxial compression loading (see **Figure 2**(b)). A tension cut-off criterion (with no softening branch) characterises the spring response in tension/flexure, while shear-governed behaviours are reproduced using a Mohr-Coulomb-like model, where cohesion is set to zero right after reaching the maximum shear strength, as shown in **Figure 2**(c).

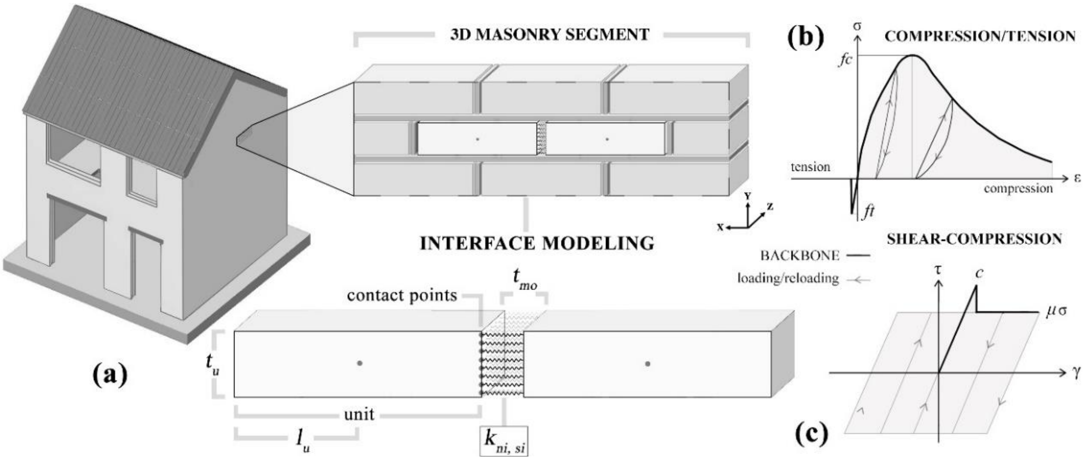

Figure 2. (a) Adopted AEM discretisation of a masonry cell and spring interface stiffnesses, (b) compression/tension and (c) shear-compression joint models (adapted from Malomo et al. 2020a)

To reproduce joint-level failure modes, the mechanical properties of each masonry component needs to be determined, selected, and assigned to the associated normal/shear interface springs. However, experimental campaigns rarely include all the necessary tests for characterising the response of mortar and units separately. Therefore, as suggested by Malomo et al. (2019b), a number of empirical (i.e. Jäger et al. 2004; Kaushik et al. 2007) and theoretical (i.e. Brooks and Baker 1998; Ciesielski 1999; Matysek and Janowski 1996; U.B.C. 1991) formulae were employed to obtain first estimates of the required material parameters where direct experimental values were not available. Then, the ensuing average is considered for modelling purposes and the associated shear moduli are obtained assuming material isotropy (these values will be given in the next sections, together with the experimental ones). Using this simplified procedure, whose effectiveness has been already extensively investigated by the authors in the context of the same experimental campaign and with respect to the modelling of both static and dynamic tests on small-scale samples, in-plane and OOP-loaded components (Malomo et al. 2020b), and full-scale building specimens with cavity walls (Malomo et al. 2020a), a reasonable approximation (i.e. 0.178 s) of the undamaged state period associated to the 1st mode (i.e. 0.170 s) of EUC-BUILD6 was obtained.

During the analysis, no external dynamic relaxation schemes were introduced, meaning that the only source of damping in the proposed numerical models is the energy dissipation due to difference in loading and unloading paths of compression springs, as well as that induced by the process of crack closure/opening. Recent applications (e.g. (Papantonopoulos et al. 2002; Calvi et al. 2019) shown that this usually provides adequate results when considering the collapse modelling of both reduced and large-scale systems. Interested readers may refer to Tagel-Din (1998) for additional details. The AEM formulation also readily allows the assignment of equivalent mechanical properties to interface springs to describe the actual behaviour of a wide range of connection types (e.g. nailed, friction, etc.) present in the EUC-BUILD6 building specimen, whose test results were used in this work as a reference for calibrating the AEM models considered in the numerical study presented in the following sections. Since experimental evidence has shown that the latter may influence significantly the dynamic response of cavity wall systems (see Graziotti et al. 2017; Tomassetti et al. 2019a, b), most of these details, as summarised below and illustrated in **Figure 3**, were duly reproduced in the numerical models:

- During the construction of EUC-BUILD6, the mortared connections among the underneath of the 1st floor RC slab (herein modelled as fully rigid, since no damage was observed experimentally) and the top edge of the CS longitudinal façades were filled only after the attainment of gravity loads, which thus acted only on the transversal CS façades. Consequently, the frictional resistance provided by these mortar layers is likely to be limited due to lack of vertical compression; similarly, their compressive strength might be also likely affected by shrinkage phenomena. To account for these aspects, reduced flexural and shear stiffnesses have been allotted to the corresponding interface springs (see **Figure 3**(a)). Further, for reproducing the experimental conditions in the static range, the top course of bricks of the transversal façades was deleted – and then restored – after the application of gravity loads.

- Tie connectors (i.e. 3mm-diameter and 200mm-long steel bars weakly coupling the response of CS and CL panels) and L-shaped anchors (employed during the considered test for preventing early OOP failure of roof-gable assemblies) were idealised as elastic-perfectly-plastic beam elements; their numerical distribution faithfully replicates the actual one (i.e. 1 tie/m^2). In the AEM model, to avoid the explicit simulation of interpenetration phenomena (such as the pull-out) between ties and masonry leaves and reduce computational expense, the contact with masonry occurs only through the transverse section of the ties (see **Figure 3**(b)). Since they typically failed within the CL mortar bonds, a strain-softening bilinear constitutive law (with pull-out strength equal to the experimentally inferred one, i.e. 2.3 kN, see Messali et al. 2016) was assigned to the CL wall-tie interfaces. Contrarily, on the CS wall side, a linear elastic connection, characterised by the CS mortar flexural stiffness, was used.

- The roof structure of EUC-BUILD6 consisted of an assembly of timber joists and planks covered by ceramic tiles (see **Figure 3**(d)), whose nonlinear response was mainly governed by the mechanical contribution of nailed connections. While timber members have been explicitly modelled as elastic elements for representing URM walls-ties, the system nonlinearity was accounted for by equivalent interface springs with initial and post-peak rotational stiffnesses (i.e. $k_{\varphi 0}$ and $k_{\varphi 1}$, determined according to Gattesco and Macorini 2014, assumed as 1773 and 77 kNmm/rad respectively), in which the system nonlinearity is lumped, and characterised by a strain-hardening bilinear constitutive law, as described by Foschi (1974). In practice, through the definition of F_{max}, namely the maximum lateral capacity (equal to 1.3 kN) experimentally-inferred by Dolan and Madsen (1992), the value of $k_{\varphi 0}$ automatically changes into $k_{\varphi 1}$ right after reaching F_{max}.

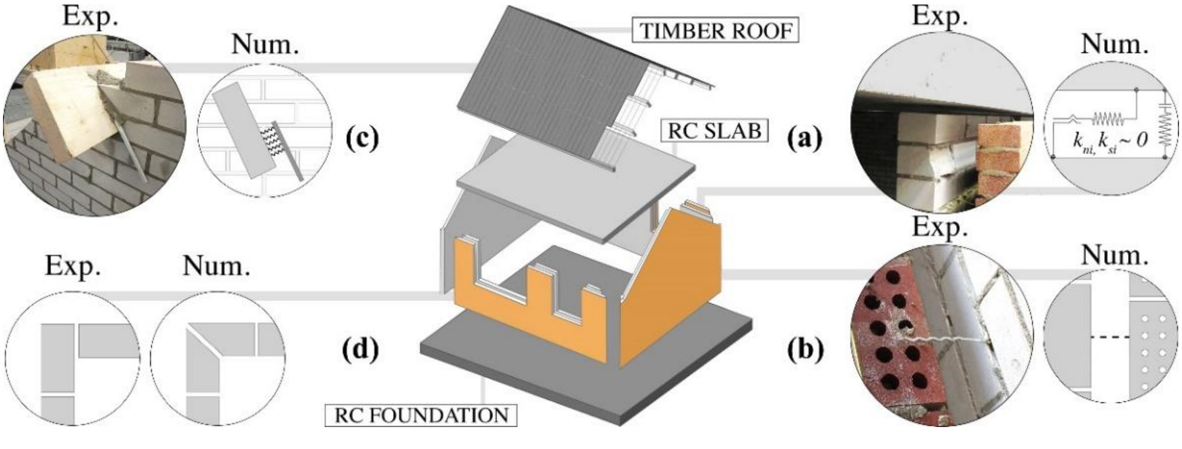

Figure 3. Experimental vs. numerical construction details of terraced house test specimen (adapted from Malomo et al. 2020a)

3. SIMULATION OF THE SHAKE-TABLE BEHAVIOUR OF A CAVITY WALL BUILDING SPECIMEN

The EUC-BUILD6 building prototype (see **Figure 4**) was tested at the shake-table of Eucentre and, as extensively discussed in (Miglietta et al. 2019), and consisted of a two-storey URM structure with asymmetrically-distributed large openings (particularly at the ground floor), RC diaphragms, timber roof and cavity walls. It was 5.94 m large, 5.58 m wide and 7.83 m-height, with a total mass of 47.2 tons. Considering the definition reported in the Groningen Exposure Database by Arup (2019a), according to which the opening percentage can be computed as the ratio between the width of the openings and the width of the façade, the longitudinal ground floor walls of EUC-BUILD6 are characterised by 80% (West) and 50% (East) opening percentages, while the South façade was built as a blind wall, since the specimen was meant to represent the end-unit of a set of terraced house systems.

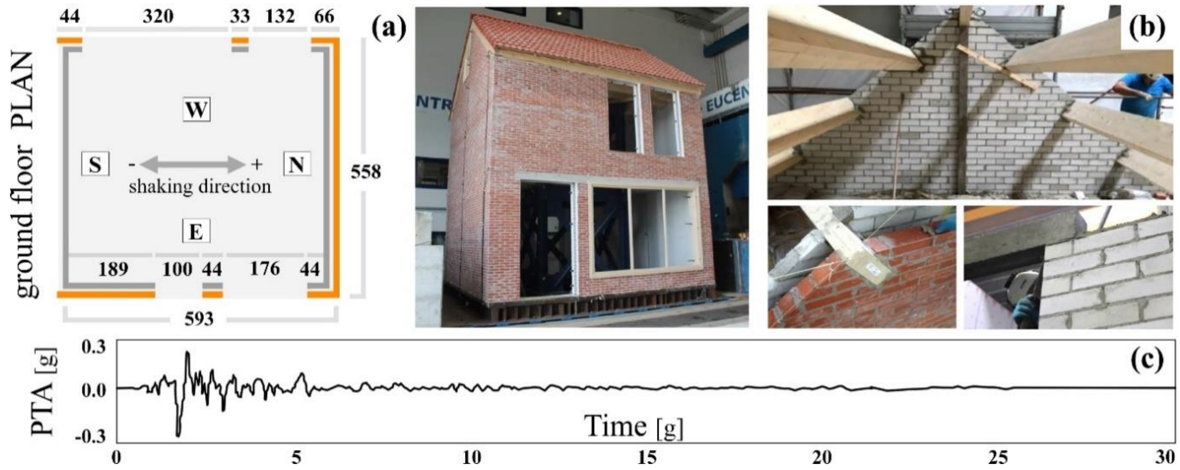

Figure 4. (a) Ground floor plan (in cm), (b) EUC-BUILD6 and roof construction details (Miglietta et al. 2019) (c) and unscaled acceleration time-history (i.e. EQ-100%, plotted as peak table acceleration-PTA vs time)

The building prototype was fixed to the shake-table and the acceleration time-history depicted in **Figure 4**(c), scaled according to the uniaxial loading protocol reported in **Table 1** (where PTA is peak table acceleration), together with the damage limit states identified by Miglietta et al. (2019), was incrementally applied until reaching near-collapse condition.

Table 1. Test loading protocol, damage evolution and limit states of EUC-BUILD6 (Miglietta et al. 2019)

Test ID	PTA [g]	Damage limit states [-]	Test ID	PTA [g]	Damage limit states [-]
EQ-20%	0.06	DL_1 – no visible damage	EQ-85%	0.25	DL_2 – minor str. damage
EQ-33%	0.14	DL_1 – no visible damage	EQ-100%(a)	0.30	DL_2 – minor str. damage
EQ-50%	0.15	DL_1 – no visible damage	EQ-100%(b)	0.29	DL_3 – damage in all the CS piers
EQ-66%	0.22	DL_2 – minor str. damage	EQ-133%	0.38	DL_4 – near-collapse conditions

In **Table 1**, the main masonry material properties (i.e. compressive strength of masonry fc_m, flexural bond strength f_w, cohesion c and friction coefficient μ), obtained either using the analytical formulae mentioned above or through characterisation tests and directly implemented in the model, are summarised:

Table 2. Actual and analytically-inferred masonry material properties of EUC-BUILD6

	CS - density $\delta_m = 1837$ [kg/m^3]								CL - density $\delta_m = 1967$ [kg/m^3]							
	fc_m	fc_u	f_w	E_m	c	μ	^1E_u	$^2E_{mo}$	fc_m	fc_u	f_w	E_m	c	μ	^1E_u	$^2E_{mo}$
Avg [MPa]	10.1	19.8	0.28	6593	0.6	0.7	7029	6593	11.6	50.0	0.24	4436	0.3	0.6	9000	1126
C.o.V. [%]	0.06	0.18	0.32	0.09	-	-	0.4	-	0.29	0.10	0.52	0.29	-	-	0.2	-

[1] derived analytically using the equations proposed by Jäger et al. (2004) and Kaushik et al. (2007)

[2] inferred according to Brooks and Baker (1998), Ciesielski (1999), Matysek and Janowski (1996) and U.B.C. 1991

With respect to the observed response of the specimen, it should be noted that flexural/rocking mechanisms were predominant, as exhaustively discussed in Miglietta et al. (2019), with the first significant cracks detected at EQ-50% in the longitudinal CS panels/spandrels. No damage was observed at this stage in the CL walls. After EQ-85%, where both CS and CL transverse walls developed some cracks at the first floor due to the activation of an

OOP mechanism, extensive damage was detected at EQ-100% due to increase in the width of pre-existing cracks and the activation of OOP two-way bending mechanisms in the first-floor transversal walls. Only moderate damage was experienced, instead, by the CL façades. The test was stopped right after EQ-133%, where the majority of the previous cracks substantially increased their extension/width, i.e. when the specimen reached near-collapse condition (determined by visual inspection). It is noted that the latter was considered as a collapse-prevention threshold, characterised by heavy global structural damage, after which the repair of a house in similar conditions may not be convenient. From a numerical viewpoint, the analysis was interrupted right after the end of the last experimentally-performed shaking sequence. In **Figure 5**(a), a comparison between actual and numerical floor and roof displacements, expressed in the form of interstorey drift ratios δ^{1st}, δ^{2nd}, δ^{roof} (computed as the relative displacement of the considered floor/roof diaphragm divided by the storey/roof height underneath), whose maximum values (starting from EQ-50%, i.e. when nonlinear response became predominant) are also summarised in **Figure 5**(b), is proposed. The model captured satisfactorily the experimentally-observed displacement demand at both floor and roof levels, although minor differences were predicted especially in the final test phases, where the model marginally overestimated and underestimated the 2nd floor and roof deformation capacities along positive and negative direction respectively. In the same figure, the factors *rBSc* and *rδ* are reported in table form. They are defined as the ratio between actual and predicted base shear coefficient BSc (calculated as the ratio between the absolute maximum recorded overall base shear and the weight of the specimen) and floor/roof interstorey drift ratios, indicate whether the model is under (red colour)-or over (light blue colour)-estimating the actual response. The general positive impression regarding the model performance is further confirmed from the hysteresis curves shown in **Figure 5**(c), where adequate agreement was found also in terms of dissipated energy and total base shear. Additional details (e.g. hysteresis curves and damage evolution for each test phase, not reported in this work due to space constraints) can be found in (Mosayk 2019).

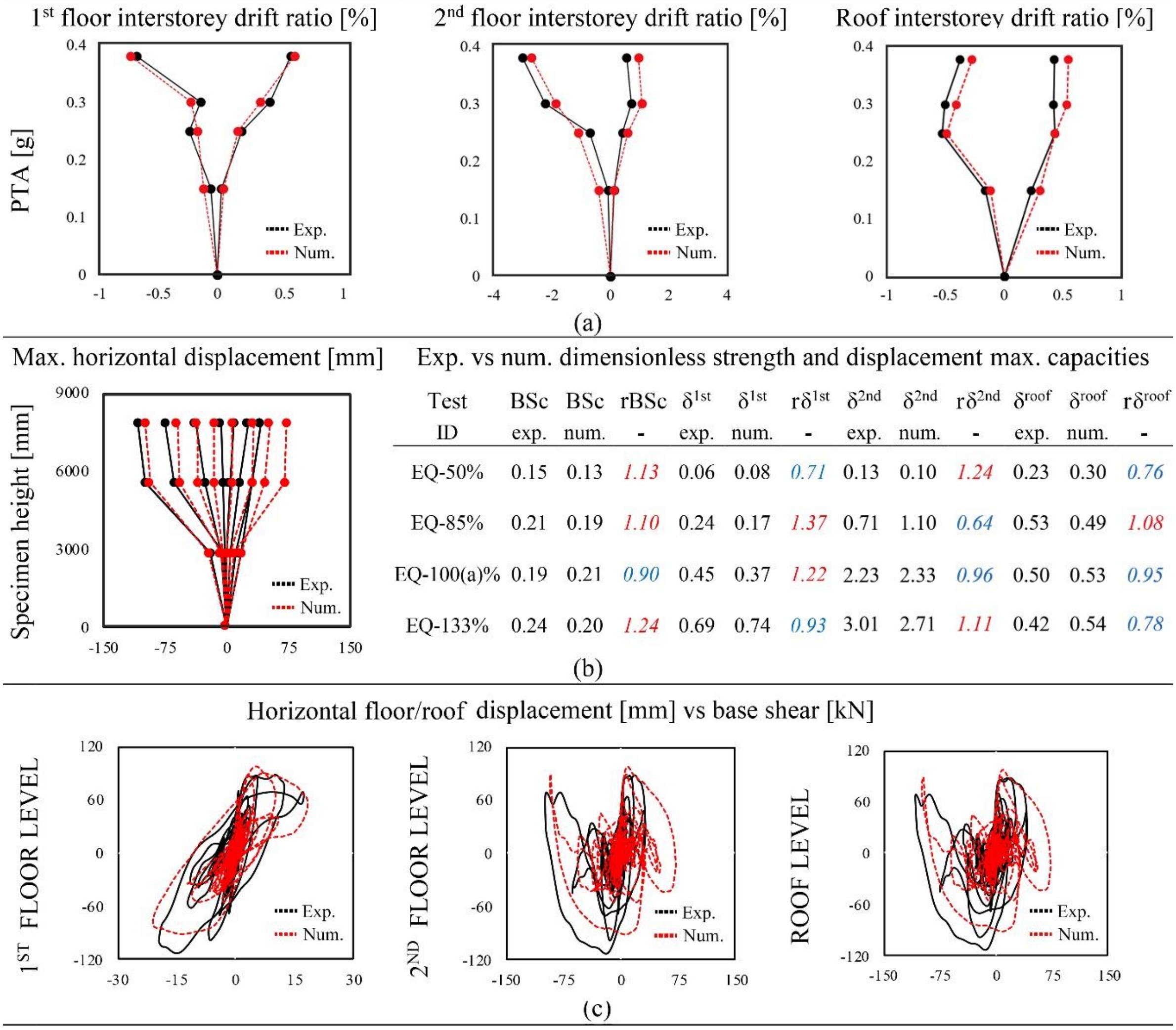

(a)

Exp. vs num. dimensionless strength and displacement max. capacities

Test ID	BSc exp.	BSc num.	rBSc -	δ^{1st} exp.	δ^{1st} num.	$r\delta^{1st}$ -	δ^{2nd} exp.	δ^{2nd} num.	$r\delta^{2nd}$ -	δ^{roof} exp.	δ^{roof} num.	$r\delta^{roof}$ -
EQ-50%	0.15	0.13	*1.13*	0.06	0.08	*0.71*	0.13	0.10	*1.24*	0.23	0.30	*0.76*
EQ-85%	0.21	0.19	*1.10*	0.24	0.17	*1.37*	0.71	1.10	*0.64*	0.53	0.49	*1.08*
EQ-100(a)%	0.19	0.21	*0.90*	0.45	0.37	*1.22*	2.23	2.33	*0.96*	0.50	0.53	*0.95*
EQ-133%	0.24	0.20	*1.24*	0.69	0.74	*0.93*	3.01	2.71	*1.11*	0.42	0.54	*0.78*

(b)

(c)

Figure 5. (a) Experimental vs numerical comparisons in terms of (a) interstorey drift ratio curves, (b) building displacement profile and dimensionless strength-displacement absolute max. capacities, (c) total floor/roof displacement vs total base shear hysteretic curves

As may also be gathered from **Figure 6**, actual and numerical final crack patterns are comparable (only numerical cracks with width > 1 mm were displayed), even if the model slightly underpredicted the damage propagation in the spandrel elements and the OOP-loaded transversal CS walls, particularly in the gables, where an overturning failure mechanism (more pronounced than its experimental counterpart) was obtained numerically. Similarly, probably because of the simplified modelling strategy presented in Section 2, the extent of horizontal cracks in the CS walls (which are may be due to the dynamic interaction among masonry and embedded tie connectors) were not adequately captured by the model. As observed experimentally, flexure/rocking failure mechanisms were predominant, with most of the damage concentred at the base/top joints of longitudinal piers, as well as in the CS transversal walls under two-way bending OOP actions. Further, it is worth noting that the crack localisation experienced by the specimen at the intersection between West and North façades, which might be caused by a torsional mechanism induced by the asymmetrical distribution of large openings in the longitudinal panels, was explicitly represented by the model.

For future comparisons, it is worth mentioning that performing the whole incremental dynamic analysis took 10–12 h (CPU: Intel Core i7 7820x, RAM: 64 GB DDR4, SSD: 250 GB M2-960-EVO), which seems reasonable especially if compared with other micro-modelling approaches (e.g. Çaktı et al. 2016; Galvez et al. 2018a).

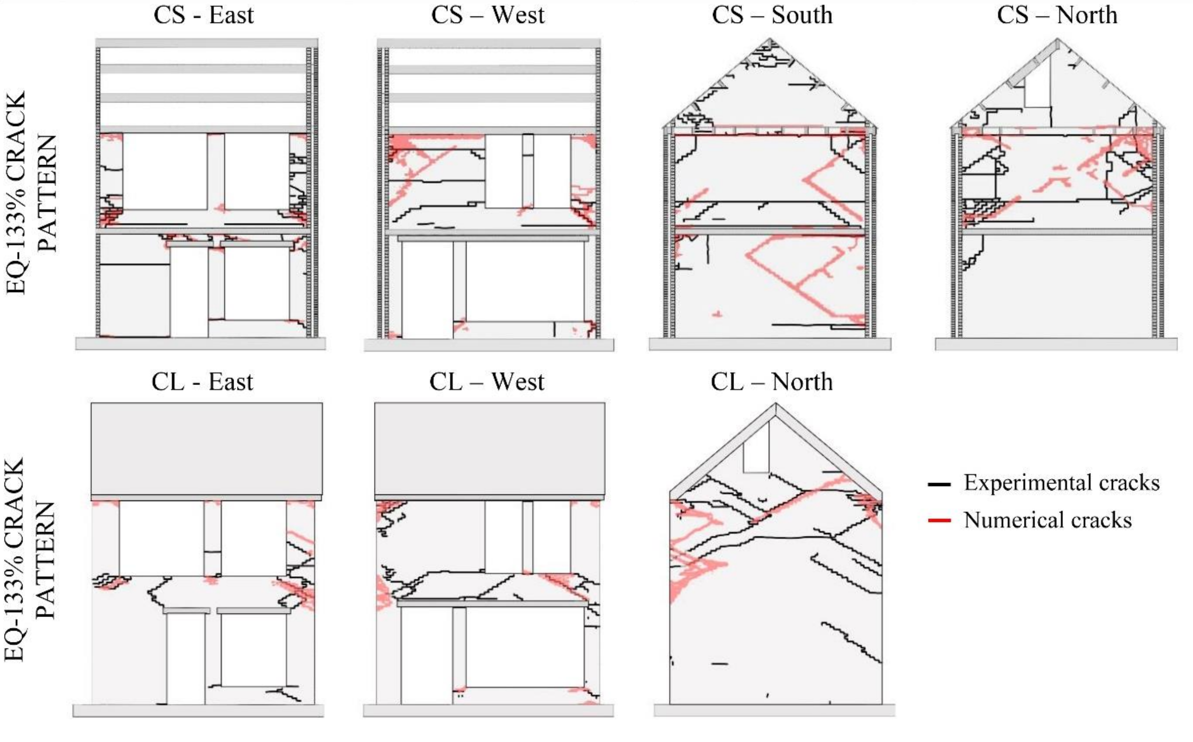

Figure 6. Experimental vs numerical final crack pattern (predicted cracks with width > 1mm coloured in red)

4. INFLUENCE OF GROUND FLOOR OPENING PERCENTAGE ON DYNAMIC RESPONSE

In this section, a numerical study on the influence of ground floor openings percentage (it is recalled that the latter is herein defined as the ratio between the width of the openings and the length of the façade) on the seismic response of a cavity wall URM structure such as the tested house (i.e. EUC-BUILD6), is proposed. To this end, the calibrated EUC-BUILD6 model previously described (which featured 80% and 50% ground floor openings percentage in the West and East direction respectively) was geometrically modified to consider different configurations, characterised by various ground opening layouts (it is noted that the lower- and upper-bound opening percentages derive from the Groningen building exposure data reported in Arup (2019a)). In the first sub-section, the same incremental dynamic loading protocol employed in the test (which was again applied consecutively, i.e. accounting for the effect of damage accumulation) of EUC-BUILD6 was considered, as well as the same modelling assumptions. Finally, taking advantage from the findings of the latter modelling exercise, a number of triaxial acceleration time-histories (selected to cover a range of intensities, as discussed in the following) were imposed to the model (each record was herein applied individually), thus enabling a broader and more realistic investigation of the effect that the ground floor opening percentage may have, also in terms of collapse capacity.

4. 1 EXPERIMENTALLY-EMPLOYED INCREMENTAL UNIAXIAL ACCELERATION TIME-HISTORIES

Two geometrical configurations, which can be deemed as representative of a lower and upper bound with reference to the extent of ground floor openings of the shake-table-tested prototype, as described below in more detail and graphically represented in **Figure 7**, are considered in this sub-section. The obtained numerical results are compared to those experimentally-inferred from the shake-table test of EUC-BUILD6 (hereinafter referred to as GF080). It is noted that the ratio between the openings percentage of West and East façades was kept, in as much as possible, in the range of the one of EUC-BUILD6, i.e. approximately 1.6.

- Configuration GFO50 – in this case, rather than increasing the openings percentage of the initial structure, these were initially decreased to the following values: 50% for the West façade and 30% for the East façade
- Configuration GFO90 – keeping again constant the ratio between the openings percentage of West and East façade, the openings percentage was increased up to 90% and 60% for West and East façade respectively

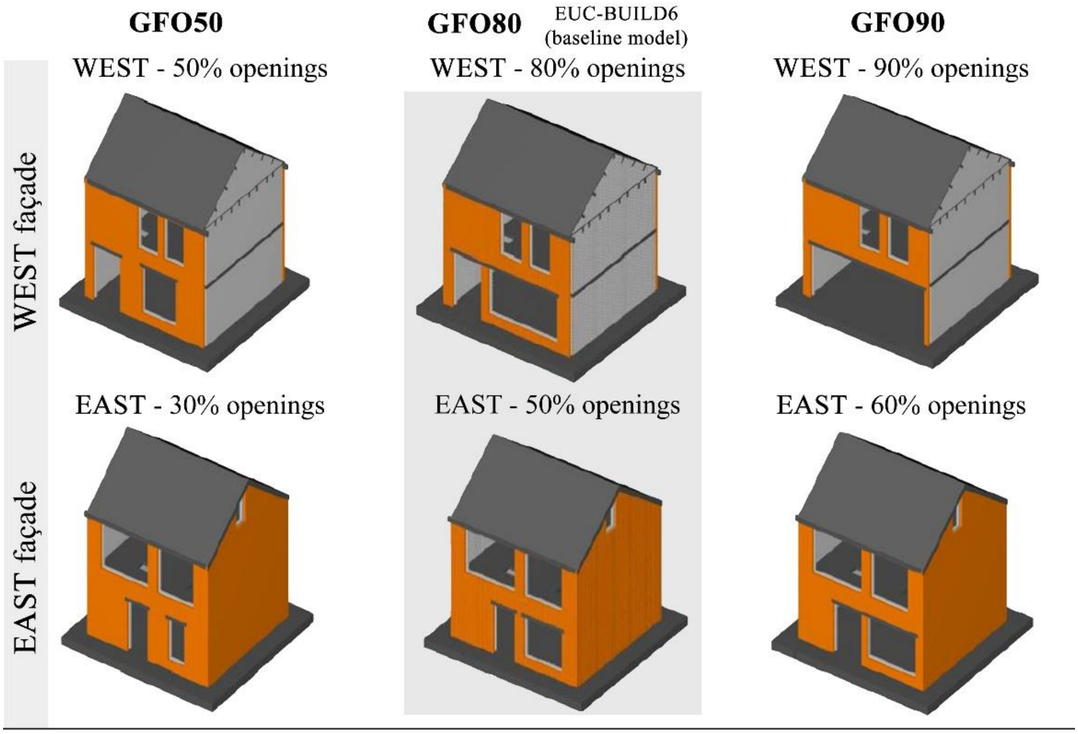

Figure 7. Screenshot of the models subjected to the experimentally-employed incremental uniaxial acceleration time-histories

In what follows, predicted responses for the two configurations described above are compared to each other, as well as to the experimental outcomes of the baseline structure (i.e. GFO80), allowing one to readily gather the impact that modifying the façade layout varying percentage of openings has on the response of the building prototype. As shown in **Figure 7**(a), the lateral drift capacity of the various models markedly decreases with increasing openings percentage. Indeed, in the case of GFO50, where the ground floor openings percentage has been reduced, the predicted first floor displacement along the negative direction of loading (i.e. South, where the CL transversal wall is not present) is almost 5 times smaller than the one of the baseline model and more than 15 times lower with respect to that predicted in the case of GFO90. The second floor and roof displacements for the various configurations considered, instead, appear comparable (albeit differences ranging from 20% for the second floor to 30% for the roof level were observed among e.g. GFO80 and GFO50 model). This is because the models experienced different failure modes, somehow counter-balancing the expected dissimilarities. As can be gathered from **Figure 9**, where the predicted damage propagation for all the configurations are compared, and further discussed in the following, the much more flexible characteristics of the ground floor level of GFO90 inevitably transformed the significantly stiffer response of the latter into that of a first-floor soft-storey type. Contrarily, in the cases of GFO80 and the GFO50 model, the stiffer response of the ground floor resulted in a damage localisation at the second-floor, thus this time inducing a second-floor soft-storey mechanism.

From the hysteresis curves depicted in **Figure 7**(b), as for the drift capacities, it is also evident that the overall strength capacity of the specimens would tend to decrease with increasing openings percentage. Such considerations are well epitomised by the plot in **Figure 7**(c), where absolute maximum floor/roof interstorey drifts for each intensity level are plotted against the corresponding dimensionless BSc, and confirm that the extent of ground floor openings may affect significantly the dynamic performance of this specific type of URM cavity wall buildings. Finally, in **Figure 9**, the crack patterns at the end of the analyses are given (for the sake of clarity, cracks with width >1 mm are highlighted in black colour), confirming the first and second floor soft-storey types of response for GFO90 and GFO50, respectively. Indeed, the latter only suffered limited cracks at the ground floor, particularly for what concerns OOP damage in the CS transverse walls, which is close to negligible. For the cases of GFO90 a higher concentration of damage at the ground floor, instead, was observed, with several and diffuse cracks propagating on both in-plane and OOP-loaded CS/CL façades.

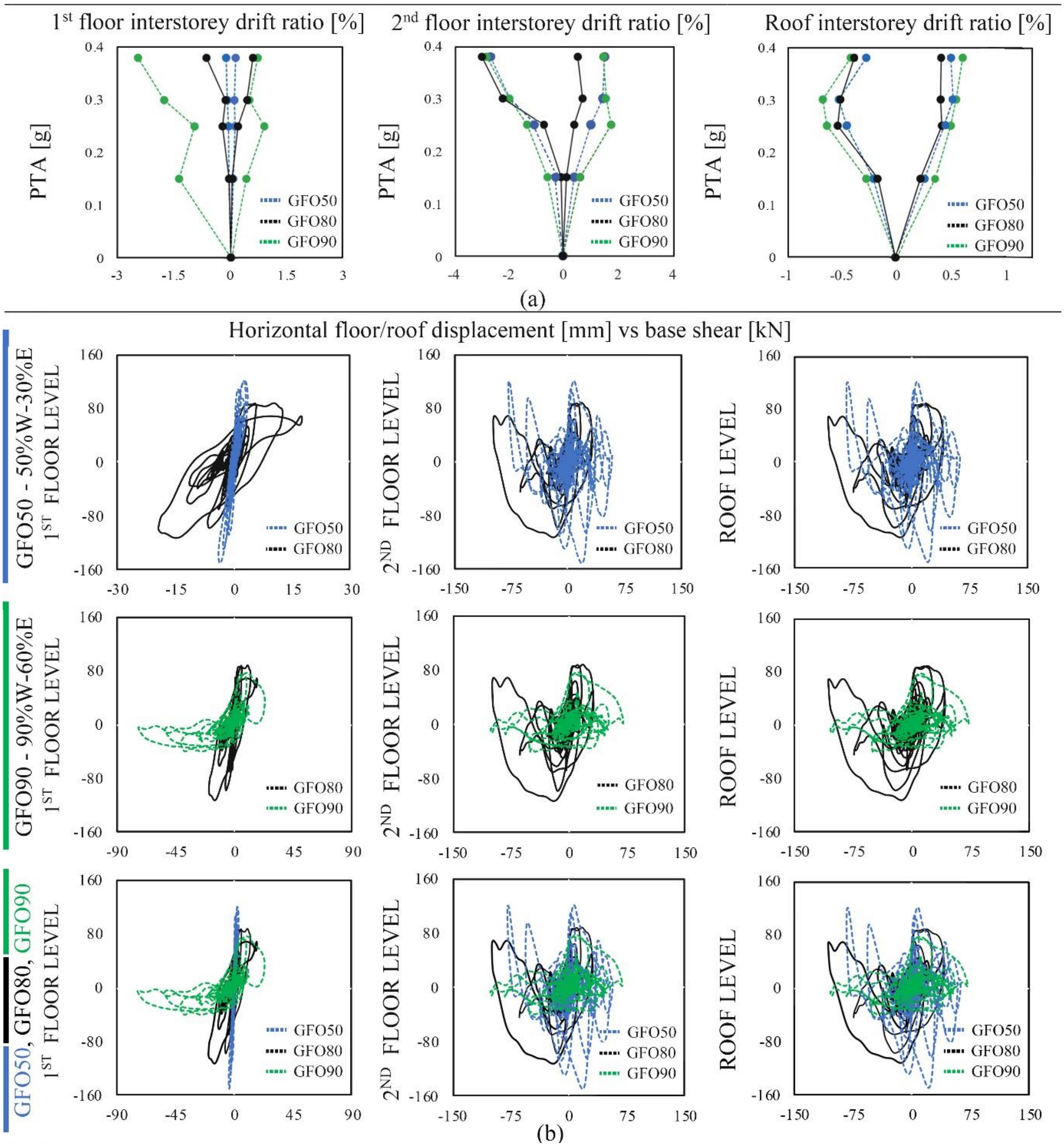

(a)

(b)

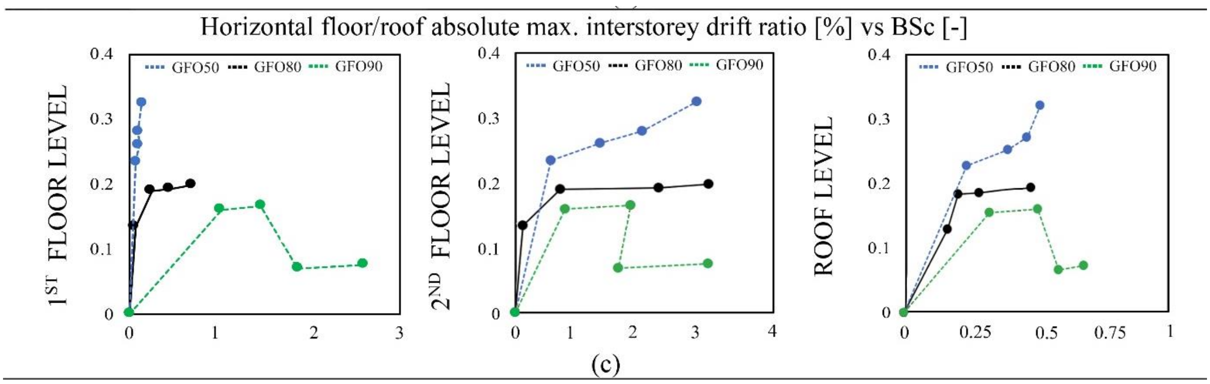

Figure 8. Experimental vs numerical results for each geometrical configuration in terms of (a) interstorey drift ratio curves, (b) floor/roof displacement vs total base shear hysteretic curves and (c) total horizontal floor/roof absolute max. interstorey drift ratio vs BSc for each intensity level

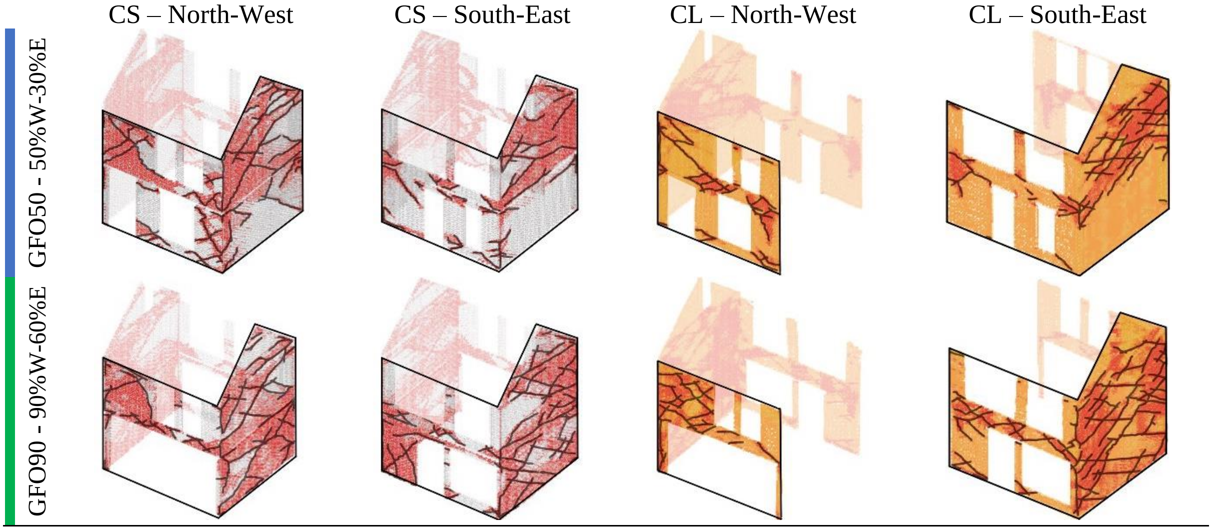

Figure 9. Numerical final crack patterns for all the configurations (cracks with width > 1mm highlighted in black colour)

4.2 TRIAXIAL ACCELERATION TIME-HISTORIES

This section focuses on the undertaking of nonlinear dynamic analyses using the 11 triaxial “training records” (see Arup, 2017) employed in the fragility functions development by Crowley et al (2019a,b). As shown in **Figure 9**, four different combinations of opening layouts were considered; an additional configuration, i.e. GFO65, with a percentage of openings of 65% (West) and 45% (East), was introduced so as to allow a more evenly spread variation of the openings percentage (it is recalled that the lower- and upper-bound opening percentages derive from the Groningen building exposure data reported in Arup (2019a)). As before, the ratio between the openings percentage of West and East façades was kept in the range of the one of GFO80, i.e. 1.6. In addition to GFO65, the following configurations were thus also selected:

- Configuration GFO50 – As for the previous sub-section, the openings percentage of the baseline model were decreased to 50% and 30% for West and East façade respectively
- Configuration GFO80 – As in the case of EUC-BUILD6 building specimen, a percentage of openings of 80% and 50% were considered on the West and East side respectively
- Configuration GFO90 – As for the previous sub-section, in this case the openings percentage was increased up to 90% and 60% for West and East façade respectively

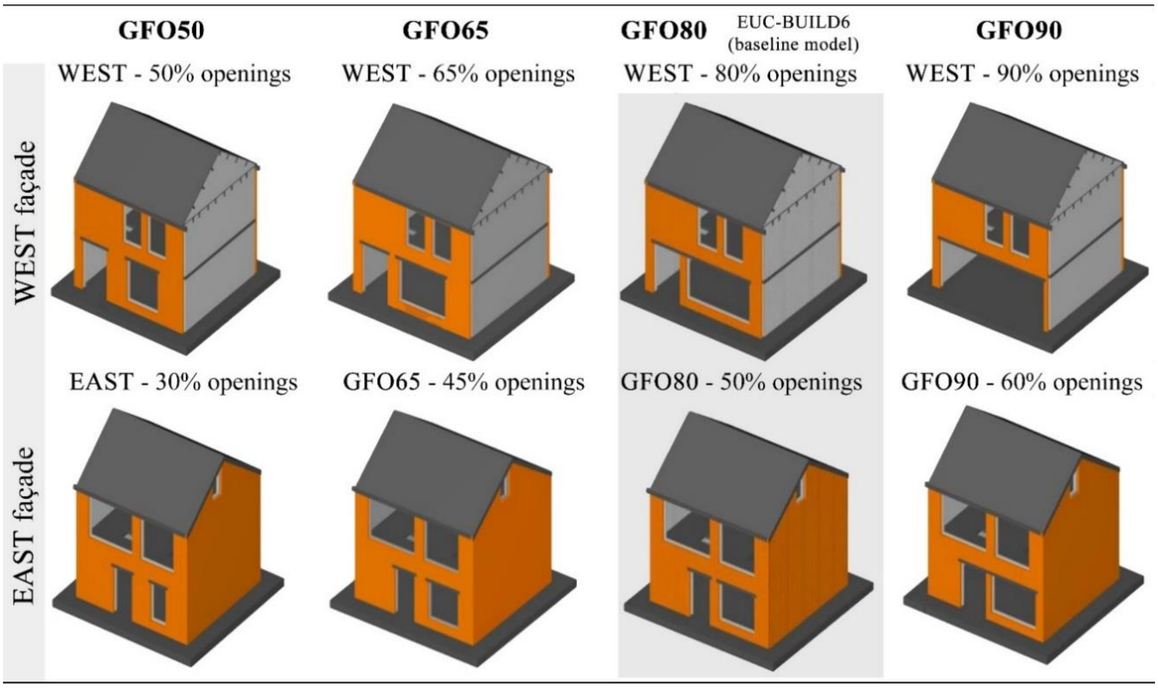

Figure 10. Screenshot of the models subjected to incremental triaxial acceleration time-histories

As already mentioned, in this case, 11 different triaxial ground motions of increasing intensity (Arup, 2019b), summarised in **Table 3**, have been applied to all models presented above. These acceleration-time histories have been selected to cover a range of intensities, herein expressed in terms of average spectral acceleration (avgSa, defined as the geometric mean of spectral accelerations from 0.01 to 1 seconds (step of 0.1 s), X direction), PGA and spectral acceleration at 0.1 seconds Sa(0.1s) along X direction (i.e. the longitudinal one, see **Figure 3**(a)).

Table 3. Main properties of the employed triaxial ground motions (Arup, 2019b)

Time-history			avgSa	Sa(0.1s)	X_PGA	Y_PGA	Z_PGA
TH no.	label	colour	[g]	[g]	[g]	[g]	[g]
1	N_00356L	🟪	0.1	0.11	0.09	0.06	0.03
2	E_00137_EW	⬜	0.25	0.44	0.19	0.32	0.10
3	N_00694T	🟦	0.34	0.38	0.23	0.24	0.08
4	N_00616T	🟦	0.41	0.49	0.24	0.14	0.18
5	N_00147T	🟩	0.48	0.67	0.25	0.19	0.17
6	N_00250L	🟩	0.71	0.87	0.88	0.41	0.32
7	E_17167_EW	🟨	0.79	0.72	0.53	0.50	0.30
8	N_00415L	🟧	1.03	1.02	0.78	1.02	0.40
9	N_00569T	🟥	1.05	0.68	0.52	0.40	0.46
10	N_00407L	🟥	1.11	1.26	0.82	0.42	0.50
11	N_00451T	🟥	1.53	1.49	1.25	0.71	0.39

The horizontal components (with peak ground acceleration X_PGA) reported in **Table 3** have been applied in the weak direction of each model (which has been identified a-priori as the longitudinal one, i.e. along the X-axis, as also confirmed by experimental outcomes), as that which is expected to have the lowest strength (i.e. lowest base shear capacity). The other two components along the Y and Z directions, characterised by Y_PGA and Z_PGA respectively, have also been applied to all models. In the following sub-sections, for the sake of clarity, the ground motions will be indicated by using the time-history numbers reported in **Table 3** (i.e. 1-11).

The AEM models predicted, depending on the considered geometrical configuration and type of imposed ground motion, a wide range of different responses, as depicted in **Figure 10** (it is noted that the roof hystereses were herein not included, given that, as shown in previous sections (see e.g. **Figure 5** and **Figure 7**), roof deformation is essentially negligible). With reference to GFO50, in several cases (e.g. records 1-2-3-4-5), giving its reduced percentage of ground floor openings, a second floor soft-storey mechanism often governed the overall behaviour, inducing significant damage localisations particularly at the first floor level. Nonetheless, although the model subjected to input 10 suffered extensive damage, also exhibiting partial collapse, only two global collapses, induced by the application accelerograms 9 and 11, were observed. The magnitude of the predicted base shear ranged from 49 (record 1) to 225 kN (record 11), corresponding to a maximum absolute 2nd floor displacement of 1.4 and 97 mm respectively. As for the case of GFO50, the numerical results obtained for GFO65 seem to indicate that a second floor soft-storey mechanism was the predominant failure mode, especially for the models subjected to the first set of ground motions (i.e. from record 1 to 5). For the remaining records, on the other hand, which are characterised by a higher value of ground acceleration, damage also propagated beneath the level of the first-floor diaphragm. Similarly to GFO50, while partial collapse was observed when imposing accelerogram 10, global failures were predicted for ground motions 9 and 11. In the latter run, it is worth noting that lower displacements, with respect to GFO50, were inferred. This might be attributable to the fact that, unlike GFO50, the failure mechanism of GFO65 also included OOP modes, which undoubtedly contributed to decreasing its displacement capacity, resulting in an early combined IP-OOP collapse (see **Figure 11**). In general, lower base shear capacities were recorded, this time ranging from 52 to 173 kN.

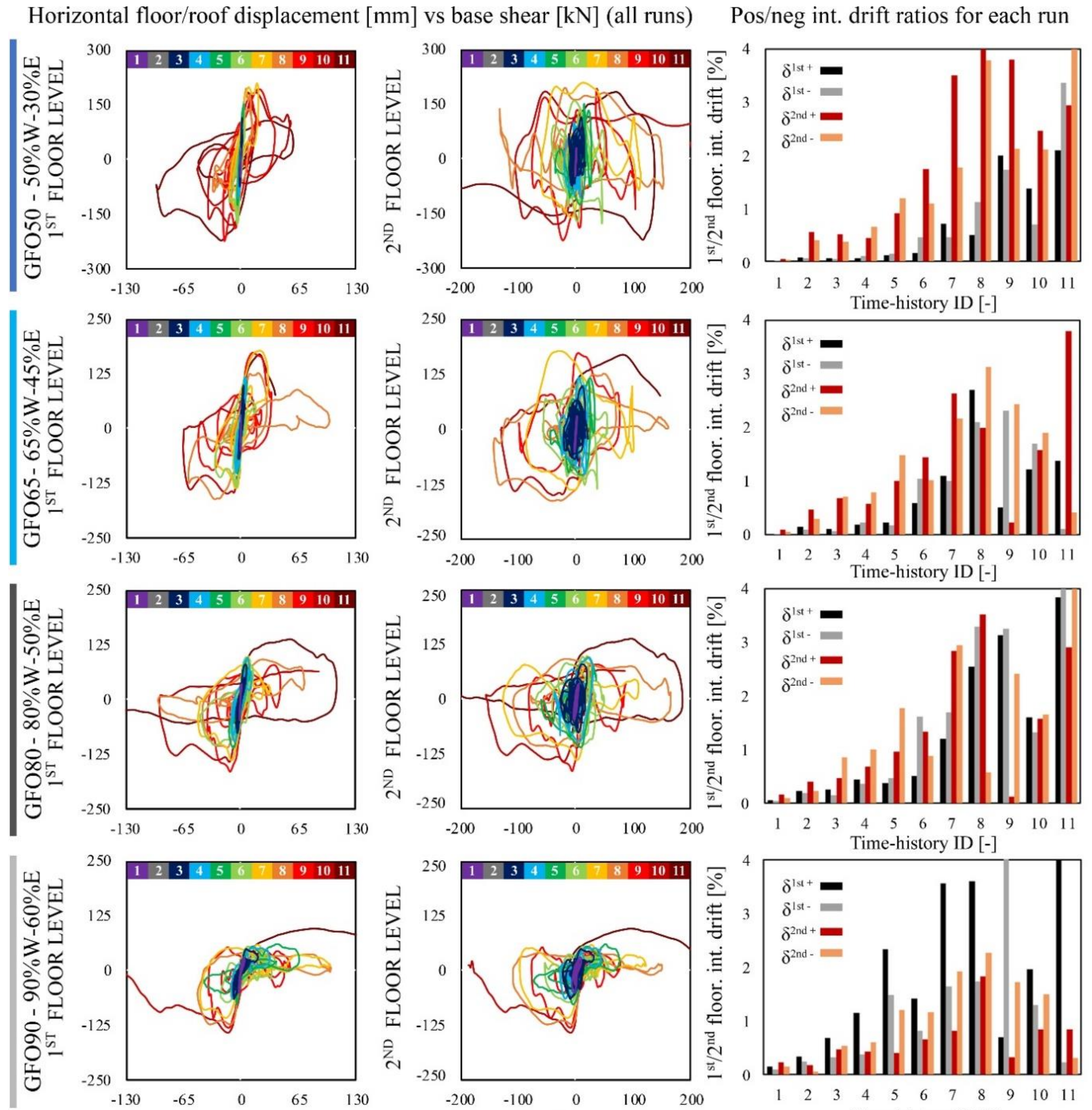

(a)

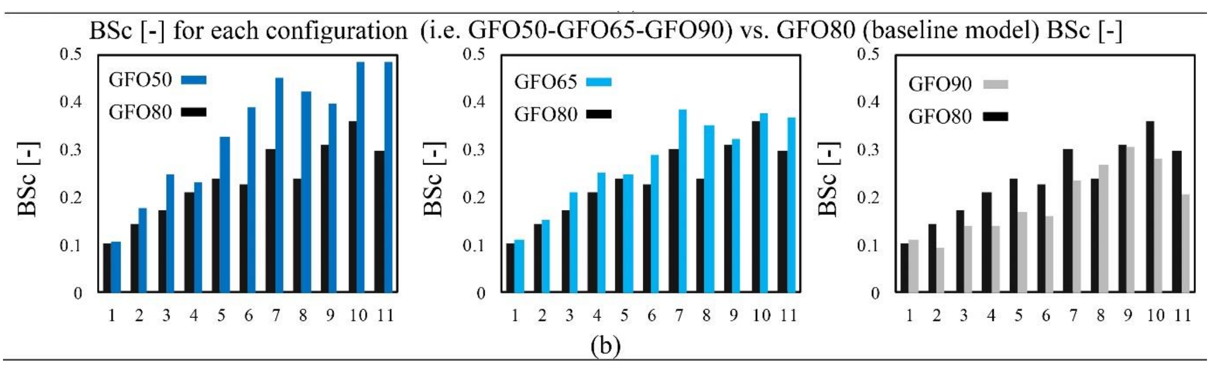

Figure 11. Numerical results for each geometrical configuration in terms of (a) total floor displacement vs. total base shear hysteretic curves and 1st/2nd interstorey drift ratios (b) BSc of GFO80 vs BSc of GFO50/GFO65/GFO90

Unlike EUC-BUILD6 (characterised by an analogous openings percentage at the ground floor of GFO80, i.e. 80% West and 50% East), the GFO80 models subjected to triaxial ground motions predicted first floor storey failure mechanisms in most of the cases. However, similarly to what has been experimentally observed in the case of EUC-BUILD6, a torsional mechanism (which also appears to be more pronounced with increasing opening percentage, as depicted in **Figure 11**), induced by the asymmetrical distribution of the large ground floor openings and causing the early failure of the CS OOP-loaded South party wall, was observed (see **Figure 11**). Further, it is noted that with respect to both GFO50 and GFO65, the extent of horizontal displacement predicted at the first floor level substantially increased, leading to a higher number of models which predicted near-collapse condition damage states and partial collapses, while the ground motions causing global collapses (i.e. record 9 and 11) and their number remained unchanged.

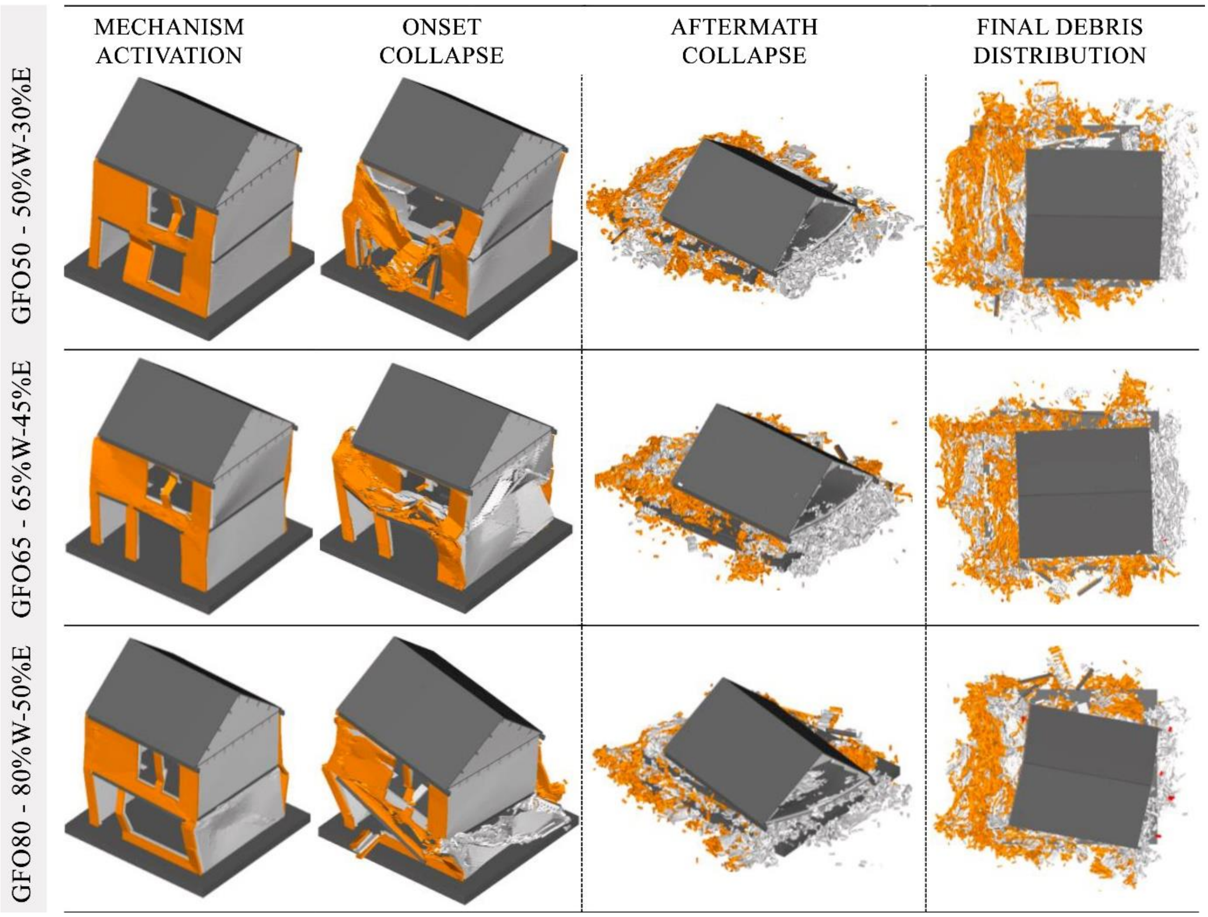

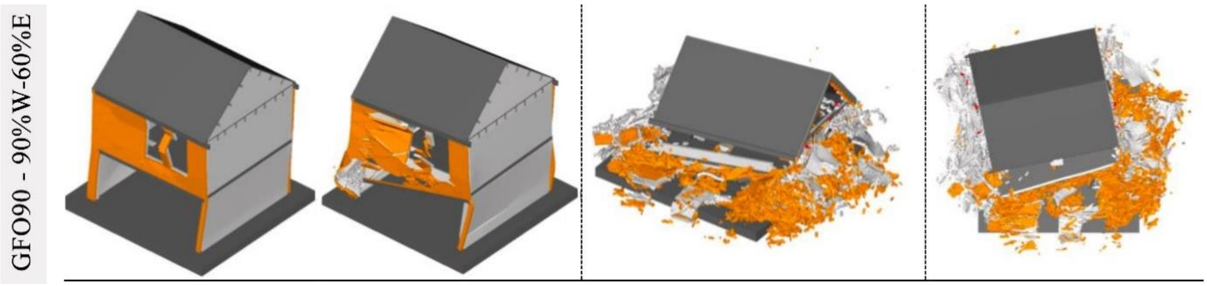

Figure 12. Selected screenshots of the most representative failure mechanisms, collapse modes and debris distribution from the considered geometrical configurations subjected to triaxial acceleration time-histories

In the extreme case of a 90% openings percentage at the West ground floor façade, as expected, a larger number of global collapses (i.e. from record 8 to 11) was predicted, with the model exhibiting a torsion-governed first floor soft-storey mechanism. With respect to all the previous configurations, a clear increase in terms of detected damage was found, even considering the first set of runs. In general, while the maximum absolute predicted base shear was significantly lower (from 44 to 130 kN), larger first and second floor displacements were observed. With a view to investigate the relationship between the extent of ground floor openings and damage level, for each analysis the latter was thus classified in the following categories (also graphically represented in **Figure 13**):

- Slight to moderate damage (S-MD): negligible or minor damage (maximum residual crack opening lower than 1 mm, as suggested in Baggio et al. 2007), easily repairable and for which the structure could be considered as fully operational
- Moderate to heavy damage (M-HD): maximum residual crack opening higher than 1mm. At this stage, which could be considered as a life safety limit state, the damage might be considered as relevant but still repairable.
- Near collapse conditions (NC): collapse-prevention threshold, characterised by heavy and widespread structural damage
- Partial collapse (PC): when the collapse of one or more members or entire sub-structures occurs, associated with heavy and widespread structural damage
- Global collapse (GC): when the entire structure experiences global failure (for the sake of clarity it should be noted that in the examples shown in **Figure 13** the onset of collapse, rather than the global collapse, is depicted)

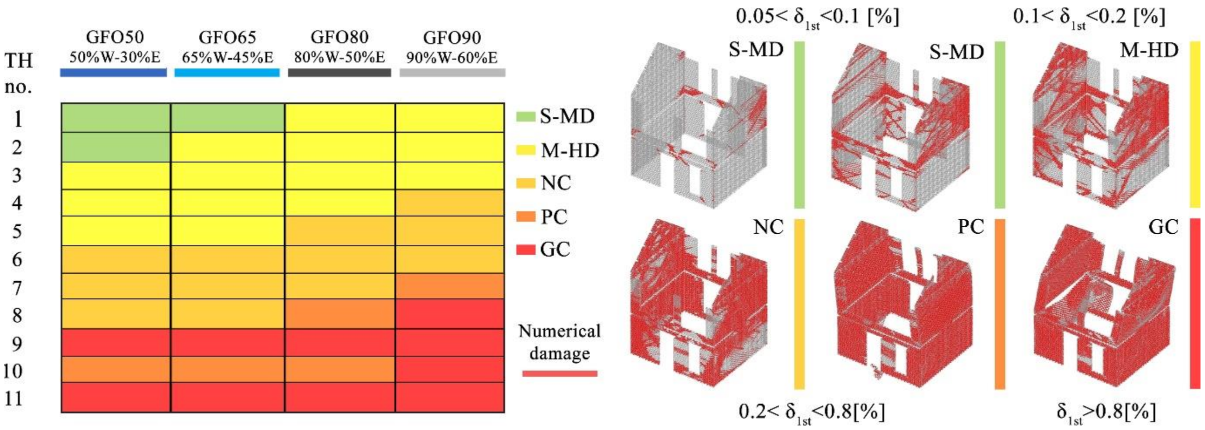

TH no.	GFO50 50%W-30%E	GFO65 65%W-45%E	GFO80 80%W-50%E	GFO90 90%W-60%E
1	S-MD	S-MD	M-HD	M-HD
2	S-MD	M-HD	M-HD	M-HD
3	M-HD	M-HD	M-HD	M-HD
4	M-HD	M-HD	M-HD	NC
5	M-HD	M-HD	NC	NC
6	NC	NC	NC	NC
7	NC	NC	NC	PC
8	NC	NC	PC	GC
9	GC	GC	GC	GC
10	PC	PC	PC	GC
11	GC	GC	GC	GC

Figure 13. Numerically-inferred damage limit states for each configuration and applied acceleration time-history, examples of crack-based identification of the proposed damage limit states

In **Figure 13**, the average range of first floor interstorey drift ratio δ^{1st} associated to each of the adopted damage limit state is also reported. It is noted that a good agreement was found with experimentally-derived drift limits for analogous structures (see e.g. Graziotti et al. 2017). As shown in in the same Figure, it seems that there is a direct relationship between the geometry of these URM cavity wall configurations, characterized by different percentages of openings at the ground storey, and their vulnerability. For what concerns the first records (i.e. 1-

5), while either S-M or M-H damage was detected when considering GFO50 and GFO65, GFO80 and GFO90 also experienced near-collapse conditions. On the other hand, focusing on the last set of records 6-11, it can be gathered that a higher number of partial and global collapses were observed in the models characterised by larger ground floor opening percentages.

5. INFLUENCE OF GROUND FLOOR OPENINGS PERCENTAGE ON FRAGILITY FUNCTIONS

In this section, for the four different configurations considered in the previous section (i.e. GFO50, GFO65, GFO80, GFO90) subjected to triaxial acceleration time-histories, fragility functions (which describe the probability of reaching/exceeding a given damage or collapse state under increasing levels of ground shaking intensity) were developed according to the procedure proposed by Crowley et al. (2019a,b). To start with, this required the definition, for each structural configuration, of a simplified single-degree-of-freedom (SDOF) system whose hysteretic response is capable of reproducing the displacement estimates that were obtained with the multi-degree-of-freedom (MDOF) AEM models under the 11 training records.

To reproduce the dynamic response using SDOF models, use was made of the software SeismoStruct (Seismosoft 2019) and the ‘multi_lin’ response curve by Sivaselvan and Reinhorn (1999) implemented therein. The latter features a polygonal hysteresis loop that can account for both stiffness and strength cyclic degradation (an example is shown in **Figure 14**a). The maximum 1st floor displacement of each of the four MDOF case-studies, under each triaxial training record, was thus converted to its equivalent SDOF counterpart (see Crowley et al., 2019a,b) and then compared with that obtained employing the SeismoStruct SDOF model. The latter was then iteratively adapted until attainment of adequate agreement between equivalent SDOF and SeismoStruct SDOF displacements *Sd*. In **Figure 14**b, such comparison, as a function of average spectral accelerations *avgSa*, for one of the structural models is depicted.

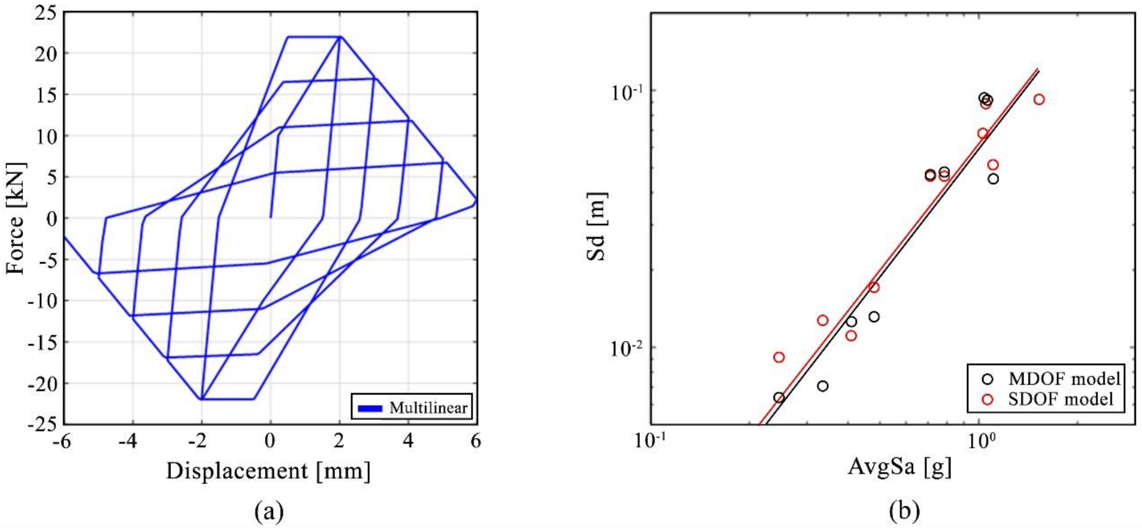

(a) (b)

Figure 14. (a) Example response curve for the *multi_lin* hysteretic model, and (b) comparison of displacements from MDOF (transformed to SDOF) and corresponding SDOF from SeismoStruct model (with calibrated *multi_lin* hysteretic response curve)

The final adopted properties for each of the four SDOF systems are reported in Table 2. The sixteen parameters of the *multi_lin* hysteretic model are defined as follows: *EI* is the initial stiffness (kN/m), *PCP* and *PCN* are the positive and negative “cracking” force (kN), *PYP* and *PYN* are the positive and negative yield force (kN), *UYP* and *UYN* are the positive and negative yield displacement (m), *UUP* and *UUN* are the positive and negative ultimate displacement (m), *EI3P* and *EI3N* are the positive and negative post-yield stiffness as percent of elastic, *HC* is the stiffness degrading parameter, *HBD* is the ductility-based strength decay parameter, *HBE* is the hysteretic energy-based strength decay parameter, *HS* is the slip parameter, and *IBILINEAR* is a model parameter equal to 0 for trilinear model, 1 for bilinear model, and 2 for vertex-oriented model.

Table 4. Final adopted properties implemented in the SDOF systems (note: *multi_lin* hysteretic model parameters are defined in base units of kN and m)

Property/Parameter	GFO50	GFO65	GFO80	GFO90
Mass (tonnes)	42	42	42	42
Period (s)	0.09	0.13	0.18	0.26
EI	200,000	100,000	50,000	25,000
PCP	100	50	50	50
PYP	160	125	125	100
UYP	0.004	0.005	0.01	0.05
UUP	0.048	0.069	0.093	0.078
EI3P	0.0046	0.008	1E-9	1E-9
PCN	100	50	50	50
PYN	160	125	125	100
UYN	0.004	0.005	0.01	0.05
UUN	0.048	0.069	0.093	0.078
EI3N	0.0046	0.008	1E-9	1E-9
HC	1	1	1	1
HBD	0.001	0.001	0.001	0.001
HBE	0.001	0.001	0.001	0.001
HS	1	1	1	1
IBLINEAR	0	0	0	0

Records compatible with the level of seismic hazard in the Groningen field at the time this study was carried out, computed with the use of the ground motion model by Bommer et al. (2017), were selected through disaggregation (mean magnitude and distance) at four different return periods (Tr = 500, 2500, 10k and 100k years) at one of the highest hazard locations in the field. The records were then selected from a large database, including European (Akkar et al., 2014) and NGA-West records (Chiou et al., 2008), and matched to spectra conditioned on four different levels of AvgSa (corresponding to the four return periods), i.e. 0.20g, 0.34g, 0.50g, 0.86g, using the ground motion selection procedure proposed by Baker and Lee (2018). The associated response spectra are depicted in **Figure 14**(a).

The cloud method (see Jalayer, 2003; Cornell et al., 2002) was then considered to derive the probabilistic relationship among ground motion intensity and nonlinear structural behaviour of the SDOF systems; once the maximum nonlinear dynamic displacement response of a given SDOF (S_{di}) is obtained from all ground-motion records, each response is plotted against a scalar/vector intensity measure (ln(*AvgSa*) herein) and the statistical parameters corresponding to a fitted lognormal distribution of $S_d \,|\, \ln(AvgSa)$ can be extracted. Specifically, the expected value, $E[\ln S_d \,|\, \ln(AvgSa)]$, is modelled by a linear regression equation (with the necessary censoring (Stafford, 2008) when the SDOF displacement response exceeds that associated with the ultimate deformation capacity obtained from the MDOF collapse analyses described earlier), whilst the standard deviation or dispersion is estimated by the standard error of the regression (see Crowley et al. (2019) for the complete formulae employed).

The final collapse fragility functions inferred for the four opening configurations considered are shown in **Figure 14**(b), confirming the observations made previously regarding the increase in seismic vulnerability of these structures when there is an enlargement of the ground-floor openings, especially accentuated when a value of 90% is reached for the ground-floor openings.

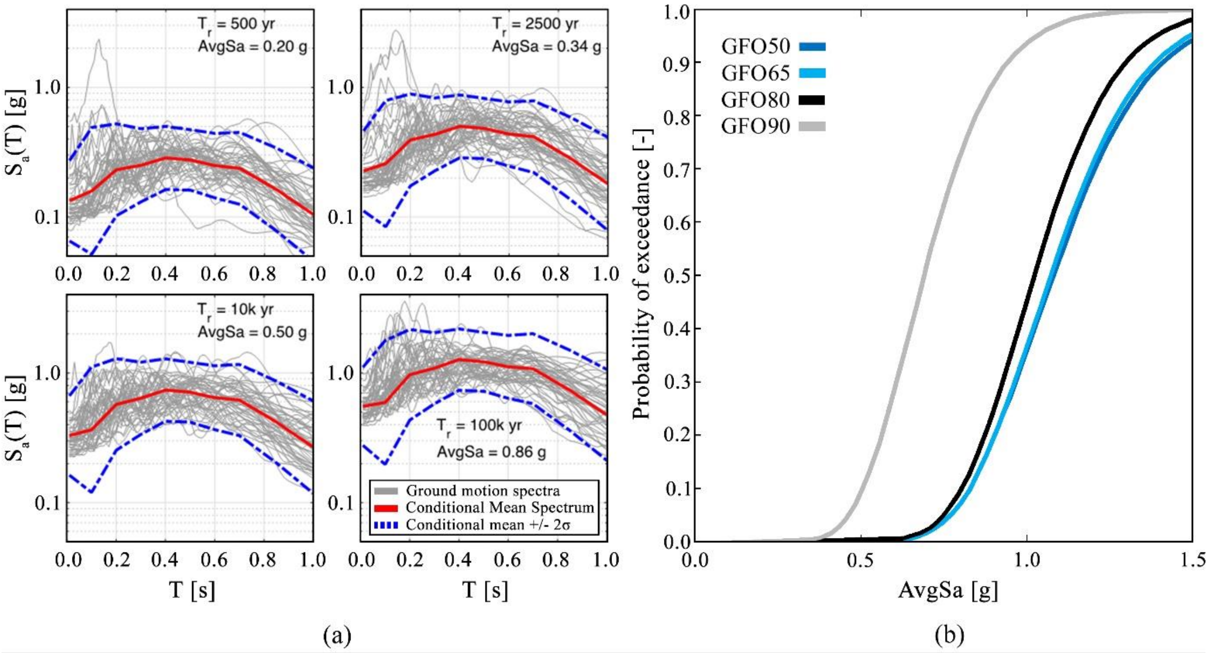

Figure 15. (a) Spectra of selected records and the conditional spectra (herein represented with the mean and +/- 2σ) to which they have been matched; (b) fragility functions inferred for each one of the four structural configurations

On the other hand, however, it can also be noticed that for the cases of 50%, 65% and 80% ground floor openings, the fragility remains relatively unchanged, which suggests that an openings percentage value in between 80% and 90% could possibly be used as a threshold for a change of fragility in this type of structures. It is underlined that, although not central to this study, where the focus is on the relative changes in fragility (as a function of ground-floor openings percentage), rather than on the absolute fragility values, the analysis of a single house unit allows a good approximation, albeit with a slight overestimation, of the seismic vulnerability of the whole terraced building, as shown in Kallioras et al. (2019).

6. CONCLUSIONS

In this work, the impact of ground floor openings percentage on the response of URM cavity wall building systems was investigated using a discrete numerical approach, the Applied Element Method (AEM), whose unique features enabled a comprehensive numerical study to be carried out in a reasonable timeframe, also accounting for IP-OOP interaction and representing explicitly damage initiation and propagation until up to complete collapse. After a preliminary calibration of the AEM model against experimental shake-table results of a full-scale cavity wall building specimen (i.e. EUC-BUILD6), where adequate agreement among actual and modelled dynamic behaviour was found, the response of a number of additional geometrical configurations, characterised by different ground floor opening percentages and subjected to various acceleration time-histories, was investigated.

The results from the first set of analyses, where the same incremental uniaxial loading protocol employed for EUC-BUILD6 was applied consecutively, i.e. accounting for the effect of damage accumulation, confirm that the extent of ground floor openings may affect significantly the dynamic performance of URM buildings, with the overall strength capacity of the latter decreasing with increasing openings percentage, which also causes deformations and failure mechanisms to concentrate on the ground floor. Similarly, when considering triaxial seismic excitation (this time without accounting for damage accumulation), it was found that the extent of damage is again proportional to the percentage of openings at the ground floor and, depending on the various selected geometrical configurations, different failure mechanisms were predicted, affecting both displacement and strength capacity. More specifically, it was observed that especially in the case of large openings percentage on the ground floor (i.e. > 80%) the overall response was significantly affected by the presence of torsional mechanisms, which governed the collapse mode, thus further increasing the vulnerability of these structural typologies towards horizontal actions. The observed torsional behaviour could perhaps have been slightly emphasized by the limitation of the analysis only to the terminal unit of the terraced house.

Leveraging upon the results of the above nonlinear dynamic analysis of the AEM models, ensuing fragility functions were also developed, allowing a more readily appreciation of how the introduction of large ground floor openings (often pursued to increase the amount of natural lighting of the house) might lead to a non-negligible increase in the seismic vulnerability of structures of the type studied in the work. A repetition of this fragility study considering one or more models of actual terraced houses will undoubtedly constitute a good complement to the results obtained here for the EUC-BUILD6 model (which, on the other hand, featured the advantage of being validated with shake-table results).

ACKNOWLEDGEMENTS

The work described in this paper was carried out within the framework of the research program on hazard and risk of induced seismicity in the Groningen region, sponsored by the Nederlandse Aardolie Maatschappij BV (NAM). The authors also acknowledge all those at both the European Centre for Training and Research in Earthquake Engineering (Eucentre, Pavia, Italy) that were involved in the testing campaign referred to in this paper, and in particular Francesco Graziotti, Gabriele Guerrini, Marco Miglietta and Luca Mazzella for their precious assistance in accessing the test data. The collaboration of the technical support staff from Applied Science International LLC (ASI), on the use of the employed AEM software - Extreme Loading for Structures, is also acknowledged. Finally, the authors are grateful to three anonymous reviewers whose insightful and constructive comments have undoubtedly contributed to a significant improvement of the overall quality of the manuscript.

REFERENCES

Akkar S, Sandikkaya MA, Senyurt M, Azari Sisi A, Ay BO, Traversa P, Douglas J, Cotton F, Luzi L, Hernandez B, Godey S (2014) Reference database for seismic ground-motion in Europe (RESORCE), Bull Earthq Eng 12:311-339.

Arup (2017) Typology modelling: analysis results in support of fragility functions—2017 batch results, Tech Rep no 229746_031.0_REP2005, November 2017. Available at http://www.nam.nl/feiten-en-cijfers/onderzoeksrapporten.html.

Arup (2019a) Exposure Database v6, Tech Rep no 229746_031.0_REP2014, 28 June 2019. Available at http://www.nam.nl/feiten-en-cijfers/onderzoeksrapporten.html.

Arup (2019b) Typology modelling: Analysis results in support of fragility functions – 2018-2019 batch results, Tech Rep no 229746_031.0_REP2015, June 2019. Available at http://www.nam.nl/feiten-en-cijfers/onderzoeksrapporten.html.

Abdulla KF, Cunningham LS, Gillie M (2017) Simulating masonry wall behaviour using a simplified micro-model approach. Eng Struct 151:349–365. https://doi.org/10.1016/j.engstruct.2017.08.021

Aref AJ, Dolatshahi KM (2013) A three-dimensional cyclic meso-scale numerical procedure for simulation of unreinforced masonry structures. Comput Struct 120:9–23. https://doi.org/10.1016/J.COMPSTRUC.2013.01.012

Baggio C, Bernardini A, Colozza R, et al (2007) Field manual for post-earthquake damage and safety assessment and short term countermeasures (AeDES). Eur Comm Res Centre—Institute Prot Secur Citizen, EUR 22868:

Brooks JJ, Baker A (1998) Modulus of Elasticity of Masonry. Mason Int 12:58–63

Çaktı E, Saygılı Ö, Lemos J V., Oliveira CS (2016) Discrete element modeling of a scaled masonry structure and its validation. Eng Struct 126:224–236. https://doi.org/10.1016/j.engstruct.2016.07.044

Calvi GM, Moratti M, O’Reilly GJ, et al (2019) Once upon a Time in Italy: The Tale of the Morandi Bridge. Struct Eng Int 29:198–217. https://doi.org/10.1080/10168664.2018.1558033

Chácara C, Cannizzaro F, Pantò B, et al (2018) Assessment of the dynamic response of unreinforced masonry structures using a macroelement modeling approach. Earthq Eng Struct Dyn 47:2426–2446. https://doi.org/10.1002/eqe.3091

Ciesielski R (1999) The dynamic module of elasticity of brick walls. In: Proceedings of the Conference of the Committee of Civil Engineering PZITB: Lublin, Poland

Crowley H, Pinho R (2017) Report on the v5 fragility and consequence models for the Groningen field

Crowley H, Pinho R, Cavalieri F (2019) Report on the v6 Fragility and Consequence Models for the Groningen Field. Report-Groningen F Seism Hazard Risk Assess Proj

Crowley H, Pinho R, van Elk J, Uilenreef J (2018) Probabilistic damage assessment of buildings due to induced seismicity. Bull Earthq Eng. https://doi.org/10.1007/s10518-018-0462-1

Crowley H, Polidoro B, Pinho R, Van Elk J (2017) Framework for developing fragility and consequence models for local personal risk. Earthq Spectra 33:1325–1345. https://doi.org/10.1193/083116EQS140M

D’Altri AM, Messali F, Rots J, et al (2019a) A damaging block-based model for the analysis of the cyclic behaviour of full-scale masonry structures. Eng Fract Mech 209:423–448. https://doi.org/10.1016/j.engfracmech.2018.11.046

D’Altri AM, Sarhosis V, Milani G, et al (2019b) Modeling Strategies for the Computational Analysis of

Unreinforced Masonry Structures: Review and Classification. Arch Comput Methods Eng. https://doi.org/10.1007/s11831-019-09351-x

Derakhshan H, Lucas W, Visintin P, Griffith MC (2018) Out-of-plane Strength of Existing Two-way Spanning Solid and Cavity Unreinforced Masonry Walls. Structures 13:88–101. https://doi.org/10.1016/j.istruc.2017.11.002

Desai N (2017) Evaluation of code provisions for design of medium rise buildings supporting brick veneer wall systems under the effect of in-plane seismic loads. Eng Struct 138:260–269. https://doi.org/10.1016/j.engstruct.2017.02.022

Dizhur D, Giaretton M, Giongo I, Ingham J (2017) Seismic retrofit of masonry walls using timber strong-backs. Struct Eng Soc J - SESOC 30:30–44

Dizhur D, Moon L, Ingham J (2013) Observed performance of residential masonry veneer construction in the 2010/2011 canterbury earthquake sequence. Earthq Spectra 29:1255–1274. https://doi.org/10.1193/050912EQS185M

Dolan JD, Madsen B (1992) Monotonic and cyclic nail connection tests. Can J Civ Eng 19:97–104

Domaneschi M, Cimellaro GP, Scutiero G (2019) A simplified method to assess generation of seismic debris for masonry structures. Eng Struct 186:306–320. https://doi.org/10.1016/j.engstruct.2019.01.092

El-Kashif KF, Maekawa K (2004) Time-dependent nonlinearity of compression softening in concrete. J Adv Concr Technol 2:233–247

Foschi RO (1974) Load-slip characteristics of nails. J Wood Sci 7:69–76

Furukawa A, Kiyono J, Toki K (2012) Numerical simulation of the failure propagation of masonry buildings during an earthquake. J Nat Disaster Sci 33:11–36

Galvez F, Giaretton M, Abeling S, et al (2018a) Discrete Element modelling of a two-storey unreinforced masonry scaled model. In: 16th European Conference on Earthquake Engineering. Thessaloniki, Greece

Galvez F, Segatta S, Giaretton M, et al (2018b) FE and DE modelling of out-of-plane two way bending behaviour of unreinforced masonry walls. In: 16th European Conference on Earthquake Engineering. Thessaloniki, Greece

Gattesco N, Macorini L (2014) In-plane stiffening techniques with nail plates or CFRP strips for timber floors in historical masonry buildings. Constr Build Mater 58:64–76. https://doi.org/10.1016/j.conbuildmat.2014.02.010

Giambanco G, La Malfa Ribolla E, Spada A (2018) Meshless meso-modeling of masonry in the computational homogenization framework. Meccanica 53:1673–1697. https://doi.org/10.1007/s11012-017-0664-7

Godio M, Beyer K (2019) Evaluation of force-based and displacement-based out-of-plane seismic assessment methods for unreinforced masonry walls through refined model simulations. Earthq Eng Struct Dyn 48:454–475. https://doi.org/10.1002/eqe.3144

Graziotti F, Penna A, Magenes G (2019a) A comprehensive in situ and laboratory testing programme supporting seismic risk analysis of URM buildings subjected to induced earthquakes. Bull Earthq Eng 17:4575–4599. https://doi.org/10.1007/s10518-018-0478-6

Graziotti F, Rossi A, Mandirola M, et al (2016a) Experimental characterisation of calcium-silicate brick masonry for seismic assessment. In: International Brick and Block Masonry Conference. Padua, Italy, pp 1619–1628

Graziotti F, Tomassetti U, Kallioras S, et al (2017) Shaking table test on a full scale URM cavity wall building. Bull Earthq Eng 15:5329–5364. https://doi.org/10.1007/s10518-017-0185-8

Graziotti F, Tomassetti U, Penna A, Magenes G (2016b) Out-of-plane shaking table tests on URM single leaf and cavity walls. Eng Struct 125:455–470

Graziotti F, Tomassetti U, Sharma S, et al (2019b) Experimental response of URM single leaf and cavity walls in out-of-plane two-way bending generated by seismic excitation. Constr Build Mater 195:650–670. https://doi.org/10.1016/j.conbuildmat.2018.10.076

Grunwald C, Khalil AA, Schaufelberger B, et al (2018) Reliability of collapse simulation – Comparing finite and applied element method at different levels. Eng Struct 176:265–278. https://doi.org/10.1016/j.engstruct.2018.08.068

Jäger W, Irmschler H, Schubert P (2004) Mauerwerk-Kalender 2004. Ernst & Sohn Verlag für Architektur und technische Wissenschaften

Kallioras S, Graziotti F, Penna A (2019) Numerical assessment of the dynamic response of a URM terraced house exposed to induced seismicity. Bull Earthq Eng 17:1521–1552. https://doi.org/10.1007/s10518-018-0495-5

Karbassi A, Nollet M-J (2013) Performance-based seismic vulnerability evaluation of masonry buildings using applied element method in a nonlinear dynamic-based analytical procedure. Earthq Spectra 29:399–426

Kaushik HB, Rai DC, Jain SK (2007) Stress-strain characteristics of clay brick masonry under uniaxial compression. J Mater Civ Eng 19:728–739

Lemos J V (2007) Discrete element modeling of masonry structures. Int J Archit Herit 1:190–213

Malomo, D., Pinho, R., and Penna, A. (2018). Using the applied element method for modelling calcium silicate brick masonry subjected to in-plane cyclic loading. Earthq Eng Struct Dyn 47(7):1610–1630.

Malomo D, DeJong MJ, Penna A (2019a) A Homogenized Distinct Macro-block (HDM) model for simulating the in-plane cyclic response of URM walls. In: 13th North American Masonry Conference. Salt Lake City, Utah, United States

Malomo D, DeJong MJ, Penna A (2019b) Distinct element modelling of the in-plane cyclic response of URM walls subjected to shear-compression. Earthq Eng Struct Dyn. https://doi.org/10.1002/eqe.3178

Malomo D, Pinho R, Penna A (2020a) Simulating the shake table response of unreinforced masonry cavity wall structures tested to collapse or near-collapse conditions. Earthq Spectra 36:554–578. https://doi.org/10.1177/8755293019891715

Malomo D, Pinho R, Penna A (2020b) Numerical modelling of the out-of-plane response of full-scale brick masonry prototypes subjected to incremental dynamic shake-table tests. Eng Struct 209:110298. https://doi.org/10.1016/j.engstruct.2020.110298

Malomo D, Scattarreggia N, Orgnoni A, et al (2020c) Numerical Study on the Collapse of the Morandi Bridge. J Perform Constr Facil 34:04020044. https://doi.org/10.1061/(ASCE)CF.1943-5509.0001428

Masi F, Stefanou I, Maffi-Berthier V, Vannucci P (2020) A Discrete Element Method based-approach for arched masonry structures under blast loads. Eng Struct 216:110721. https://doi.org/10.1016/j.engstruct.2020.110721

Matysek P, Janowski Z (1996) Analysis of factors affecting the modulus of elasticity of the walls. In: Proceedings of the Conference of the Committee of Civil Engineering PZITB: Lublin, Poland

Meguro K, Tagel-Din H (2000) Applied element method for structural analysis: Theory and application for linear materials. Struct Eng Eng 17:

Messali F, Esposito R, Maragna M (2016) Pull-out strength of wall ties. Report, TU Delft, NL

Miglietta M, Damiani N, Grottoli L, et al (2019) Shake-table investigation of a timber retrofit solution for unreinforced masonry cavity-wall buildings. In: In Proceedings of the XVIII ANIDIS Conference. Pisa University Press, Ascoli Piceno, Italy, pp 117–127

Mosayk (2019) Blind prediction modelling and analysis of EUC-BUILD6 specimen. Tech Rep - D11 (v 8 June 2019)

Pantò B, Cannizzaro F, Caliò I, Lourenço PB (2017) Numerical and Experimental Validation of a 3D Macro-Model for the In-Plane and Out-Of-Plane Behavior of Unreinforced Masonry Walls. Int J Archit Herit 11:946–964. https://doi.org/10.1080/15583058.2017.1325539

Papantonopoulos C, Psycharis IN, Papastamatiou DY, et al (2002) Numerical prediction of the earthquake response of classical columns using the distinct element method. Earthq Eng Struct Dyn 31:1699–1717. https://doi.org/10.1002/eqe.185

Penna A, Lagomarsino S, Galasco A (2014) A nonlinear macroelement model for the seismic analysis of masonry buildings. Earthq Eng Struct Dyn 43:159–179

Petracca M, Pelà L, Rossi R, et al (2017) Micro-scale continuous and discrete numerical models for nonlinear analysis of masonry shear walls. Constr Build Mater 149:296–314. https://doi.org/10.1016/j.conbuildmat.2017.05.130

Portioli FPA (2019) Rigid block modelling of historic masonry structures using mathematical programming: a unified formulation for non-linear time history, static pushover and limit equilibrium analysis. Bull Earthq Eng 1–29. https://doi.org/10.1007/s10518-019-00722-0

Pulatsu B, Bretas EM, Lourenço PB (2016) Discrete element modeling of masonry structures: Validation and application. Earthq Struct 11:563–582. https://doi.org/10.12989/eas.2016.11.4.563

Raka E, Spacone E, Sepe V, Camata G (2015) Advanced frame element for seismic analysis of masonry structures: model formulation and validation. Earthq Eng Struct Dyn 44:2489–2506

Salem H, Mohssen S, Nishikiori Y, Hosoda A (2016) Numerical Collapse Analysis of Tsuyagawa Bridge Damaged by Tohoku Tsunami. J Perform Constr Facil 30:04016065. https://doi.org/10.1061/(ASCE)CF.1943-5509.0000925

Sangirardi M, Liberatore D, Addessi D (2019) Equivalent Frame Modelling of Masonry Walls Based on Plasticity and Damage. Int J Archit Herit 13:1098–1109. https://doi.org/10.1080/15583058.2019.1645240

Seismosoft (2019) SeismoStruct– A computer program for static and dynamic nonlinear analysis of framed structures. available at: http://www.seismosoft.com

Tagel-Din H (1998) A new efficient method for nonlinear, large deformation and collapse analysis of structures. Dr Thesis, Univ Tokyo

Tomassetti U, Correia AA, Candeias PX, et al (2019a) Two-way bending out-of-plane collapse of a full-scale URM building tested on a shake table. Bull Earthq Eng 17:2165–2198. https://doi.org/10.1007/s10518-018-0507-5

Tomassetti U, Correia AA, Graziotti F, Penna A (2019b) Vulnerability of roof systems combining URM gable walls and timber diaphragms. Earthq Eng Struct Dyn. https://doi.org/10.1002/eqe.3187

Tomassetti U, Graziotti F, Penna A, Magenes G (2018) Modelling one-way out-of-plane response of single-leaf and cavity walls. Eng Struct 167:241–255. https://doi.org/10.1016/j.engstruct.2018.04.007

U.B.C. (1991) International Conference of Building Officials. Uniform Building Code. In: International conference of building officials, USA. Whittier, USA

Zhang W, Du H, Li X, et al (2016) In-Plane Seismic Performance of Chinese Traditional Rowlock Cavity Walls under Low-Cycle Loading. Int J Archit Herit 10:204–216. https://doi.org/10.1080/15583058.2015.1113334